Dynamic anisotropy in MHD turbulence induced by mean magnetic field

Cite as: Phys. Plasmas **24**, 022304 (2017); https://doi.org/10.1063/1.4975609
Submitted: 11 October 2016 . Accepted: 12 January 2017 . Published Online: 09 February 2017

Sita Sundar, Mahendra K. Verma, Alexandros Alexakis, and Anando G. Chatterjee

Dynamic anisotropy in MHD turbulence induced by mean magnetic field

Sita Sundar,[1] Mahendra K. Verma,[2] Alexandros Alexakis,[3] and Anando G. Chatterjee[2]
[1]*Institut für Theoretische Physik und Christian-Albrechts-Universität zu Kiel, Kiel 24098, Germany*
[2]*Department of Physics, Indian Institute of Technology Kanpur, Kanpur 208016, India*
[3]*Laboratoire de Physique Statistique, École Normale Supérieure, PSL Research University; Université Paris Diderot Sorbonne Paris-Cité; Sorbonne Universités UPMC Univ Paris 06; CNRS; 24 rue Lhomond, 75005 Paris, France*

(Received 11 October 2016; accepted 12 January 2017; published online 9 February 2017)

In this paper, we study the development of anisotropy in strong MHD turbulence in the presence of a large scale magnetic field B_0 by analyzing the results of direct numerical simulations. Our results show that the developed anisotropy among the different components of the velocity and magnetic field is a direct outcome of the inverse cascade of energy of the perpendicular velocity components $u_\perp$ and a forward cascade of the energy of the parallel component $\mathbf{u}_\parallel$. The inverse cascade develops for a strong B_0, where the flow exhibits a strong vortical structure by the suppression of fluctuations along the magnetic field. Both the inverse and the forward cascade are examined in detail by investigating the anisotropic energy spectra, the energy fluxes, and the shell to shell energy transfers among different scales. *Published by AIP Publishing.*
[http://dx.doi.org/10.1063/1.4975609]

I. INTRODUCTION

Magnetohydrodynamics (MHD) provides the macroscopic equations for the motion of a conducting fluid that is coupled with the electrodynamics equations. MHD flows are ubiquitous in nature, and they are observed in the interstellar medium, galaxies, accretion disks, star and planet interiors, solar wind, Tokamak etc. In such flows, the kinetic Reynolds number Re (defined as $Re = UL/\nu$, where U is the rms velocity, L is the domain size, and ν is the kinematic viscosity) and magnetic Reynolds number Rm (defined as $Rm = UL/\eta$, where η is the magnetic diffusivity) are so large that the flows are turbulent with a large continuous range of excited scales, from the largest scales where energy is injected into the smallest scales where energy is dissipated. Furthermore, in most of these systems, reasonably strong magnetic fields are known to exist, with correlation lengths much larger than those of the turbulent flow. These large-scale magnetic fields present in these systems induce dynamic anisotropy, and hence play a significant dynamical role in the flow evolution.

Resolving both the large scale magnetic fields and the small scale turbulence by direct numerical simulations is still a major challenge even with the presently available supercomputers (see Ref. 1). One of the possible simplifications around this difficulty is to model the large-scale magnetic field by a uniform magnetic field B_0, and study its effect on the small scale turbulence. This approximation simplifies the analysis of the system as it allows studying the effect of large magnetic fields on small scale turbulence without tracking down their slow evolution. For example, various features of the solar corona (e.g., the magnetic structures associated with prominence, coronal holes with their open field lines, and coronal loops) are modeled using such a "magnetofluid with mean B_0 field" approximation. Other systems of interest where such an approximation is advantageous include the solar wind, where the inertial-range fluctuations are subjected to a mean magnetic field, and fusion devices, like ITER, that involve large toroidal magnetic fields.

MHD turbulence in the presence of a mean magnetic field has been the subject of many studies.[2–6] The initial phenomenological estimates for the energy spectrum $E(k)$ based on Alfvén effects and isotropy led to the prediction of an energy spectrum $E(k) \propto k^{-3/2}$.[2,3] Verma[7,8] showed that the "random" large-scale mean magnetic field B_0 gets renormalized to yield $B_0(k) \sim k^{-1/3}$ and Kolmogorov-like energy spectrum ($E(k) \sim k^{-5/3}$). This result is also consistent with the energy spectrum derived by re-normalizing viscosity and resistivity.[9]

The presence of a large-scale mean magnetic field however supports the propagation of Alfvén waves that makes the flow anisotropic. The first studies of anisotropy by Shebalin *et al.*[4] in two-dimensional magnetohydrodynamics and by Oughton *et al.*[6] in three dimensions quantified the anisotropy by measuring the angles

$$\theta_{u,b} = \tan^{-1} \frac{\sum_k k_z^2 E_{u,b}(\mathbf{k})}{\sum_k \left(k_x^2 + k_y^2\right) E_{u,b}(\mathbf{k})}, \tag{1}$$

where $E_{u,b}$ is the velocity or magnetic field energy spectrum, and $\hat{z}$ is the direction of the mean magnetic field. In their low-resolution simulations ($k_{\max} = 32$), they employed $B_0 = 0$ to 16, and showed that strong anisotropy arises due to the mean magnetic field with the anisotropy being strongest at higher wavenumbers and thus it cannot be neglected. Phenomenological theories that take into account anisotropy, predict that the anisotropic energy spectrum scales as $k_\perp^{-5/3}$ (Ref. 10) (where $k_\perp$ is the wave number perpendicular to the mean magnetic field) or as $k_\perp^{-3/2}$.[11] Simulations of Boldyrev *et al.*[12–14] support $-3/2$ exponent, while those by Beresnyak[15–17] argue in favour of Kolmogorov's exponent $-5/3$. Thus, at present there is no consensus on the energy spectrum for the MHD turbulence.

The only case that analytical results have been derived is the weak turbulence limit where the uniform magnetic field is assumed to be very strong. In this limit, the evolution of the

energy spectrum can be calculated analytically using an asymptotic expansion[18] that leads to the prediction $E(k_\perp) \propto k_\perp^{-2}$. The predictions above however are valid only in large enough domains in which many large-scale modes along the mean magnetic field exist. In finite domains, one finds an even richer behavior. It has been shown[19–21] with the use of numerical simulations that in finite domains, three-dimensional MHD flows become quasi-two-dimensional for strong external magnetic fields. These states exhibit a high anisotropy with very weak variations along the direction of the magnetic field and resemble the two-dimensional turbulence. In fact, it can be shown that for B_0 above a critical value, the aforementioned two-dimensionalisation becomes exact,[22] with three-dimensional perturbations dying off exponentially in time. At intermediate values of B_0, however, three-dimensional perturbations are present and control the forward cascade of energy.

The degree of anisotropy in such quasi two-dimensionalized situations has been studied more recently. To quantify scale-by-scale anisotropy, Alexakis *et al.*[19,23] partitioned the wavenumber space into coaxial cylindrical domains aligned along the mean magnetic field direction, and into planar domains transverse to the mean field. Using this decomposition, Alexakis[19] studied the energy spectra and fluxes, as well as two-dimensionalization of the flow for mean magnetic field strengths $B_0 = 2$, 5, and 10. He reported an inverse energy cascade for the wavenumbers smaller than the forcing wavenumbers. Teaca *et al.*[24] decomposed the spectral space into rings, and arrived at a similar conclusion as above. Teaca *et al*. observed that the energy tends to concentrate near the equator strongly as the strength of the magnetic field is increased. They also showed that the constant magnetic field facilitates energy transfers from the velocity field to the magnetic field. In the present paper, we study in detail the development of anisotropy in such flows and relate it to the development of the inverse cascade.

The outline of the paper is as follows. We introduce the theoretical framework in Sec. I followed by details of the numerical simulations in Sec. II. Next, we discuss the anisotropic spectra in Sec. III, and energy transfer diagnostics like energy flux and shell-to-shell energy transfers in Sec. IV. Finally, we conclude in Section V.

II. SETUP AND GOVERNING EQUATIONS

We consider an incompressible flow of a conducting fluid in the presence of a constant and strong guiding magnetic field $\mathbf{B}_0$ along $\hat{z}$ direction. The incompressible MHD equations[8,25] are given below

$$\begin{aligned} \frac{\partial}{\partial t}\mathbf{u} + (\mathbf{u}\cdot\nabla)\mathbf{u} &= -\nabla P + (\mathbf{B}\cdot\nabla)\mathbf{b} + \nu\nabla^2\mathbf{u} + \mathbf{f} \\ \frac{\partial}{\partial t}\mathbf{b} + (\mathbf{u}\cdot\nabla)\mathbf{b} &= (\mathbf{B}\cdot\nabla)\mathbf{u} + \eta\nabla^2\mathbf{b} \\ \nabla\cdot\mathbf{u} = 0, \quad \nabla\cdot\mathbf{b} &= 0. \end{aligned} \tag{2}$$

Here $\mathbf{u}$ is the velocity field, $\mathbf{B}$ is the magnetic field, $\mathbf{f}$ is the external forcing, P is the total (thermal + magnetic) pressure, ν is the viscosity, and η is the magnetic diffusivity of the fluid. We take $\nu = \eta$, thus the magnetic Prandtl number $Pm = \nu/\eta$ is unity. The total magnetic field is decomposed into its mean part $B_0\hat{z}$ and the fluctuating part $\mathbf{b}$, i.e., $\mathbf{B} = B_0\hat{z} + \mathbf{b}$. Note that in the above equations, the magnetic field has the same units as the velocity field.

The above equations were solved using a parallel pseudo-spectral parallel code Ghost[26] with a grid resolution 512^3 and a fourth order Runge-Kutta method for time stepping. The simulation box is of the size $(2\pi)^3$ on which periodic boundary condition on all directions were employed. The velocity field was forced randomly at the intermediate wavenumbers satisfying $8 \le |k| \le 10$. This allowed to observe the development of both the inverse cascade and the forward cascade when they are present. The simulations were evolved for sufficiently long times so that either a steady state was reached, or until we observe a dominant energy at the largest scales due to the inverse cascade of energy (for large B_0). In the simulations, the forcing amplitude was controlled, while the saturation level of the kinetic energy is a function of the other control parameters of the system. Thus, the more relevant non-dimensional control parameter is the Grasshof number defined as $G \equiv \|\mathbf{f}\|L^3/\nu^2$, where $\|\cdot\|$ stands for the L_2 norm, and $L = 2\pi$ is the length scale of the system. Alternatively, we can use the Reynolds number $Re = \|\mathbf{u}\|L/\nu$ based on the rms value of the velocity. Note however that Re evolves in time in the presence of an inverse cascade. For further details of simulations, refer to Alexakis.[19]

We examine two different values of $B_0 = 2$ and 10. The results of these simulations were first presented in Ref. 19 and correspond to the runs R2 and R3 respectively in that work. The values of the control parameters used and of the basic observable are summarized in Table I. The runs have relatively moderate Reynolds number due to the forcing at intermediate wavenumbers. Therefore we do not focus on the energy spectra. Rather we aim to unravel the mechanisms that lead to the redistribution of energy and development of anisotropic turbulence due to the mean magnetic field.

Sections III and IV, we analyze the anisotropic energy spectra and energy transfer diagnostics using the generated numerical data by employing another pseudo-spectral code TARANG.[27] We describe the anisotropic energy spectra, as well as the fluxes and the energy transfers involving the velocity and magnetic fields, generated during the evolved state. Throughout the paper, we denote $u_\parallel = u_z$ and $\mathbf{u}_\perp = (u_x, u_y)$.

III. SPECTRA AND ANISOTROPY

First we present visualizations of the two examined flows for $B_0 = 2$ and 10 to demonstrate the anisotropy of the flow. In Figure 1, we present the iso-surfaces of the magnitude of

TABLE I. Steady-state parameters of the simulation: Grasshof number $G \equiv \|\mathbf{f}\|L^3/\nu^2$, Reynolds number $\|\mathbf{u}\|L/\nu$, kinetic and magnetic energies, $B_0/\|\mathbf{u}\|$, $r_A^{-1} = \|\mathbf{b}\|^2/\|\mathbf{u}\|^2$, kinetic and magnetic dissipation rates, anisotropic parameters A_u and A_b(see Eq. (3)). The values are obtained from single snapshots and not by time-averaging.

$Gr^{1/2}$	Re	B_0	$\|\mathbf{u}\|^2$	$\|\mathbf{b}\|^2$	$B_0/\|\mathbf{u}\|$	r_A^{-1}	$\nu\|\nabla\mathbf{u}\|^2$	$\eta\|\nabla\mathbf{b}\|^2$	A_u	A_b
2500	1.09×10^4	2	0.24	0.18	4.08	0.75	0.043	0.041	0.53	0.73
2500	1.53×10^4	10	0.47	0.012	14.6	0.026	0.015	0.0021	3.7	1.6

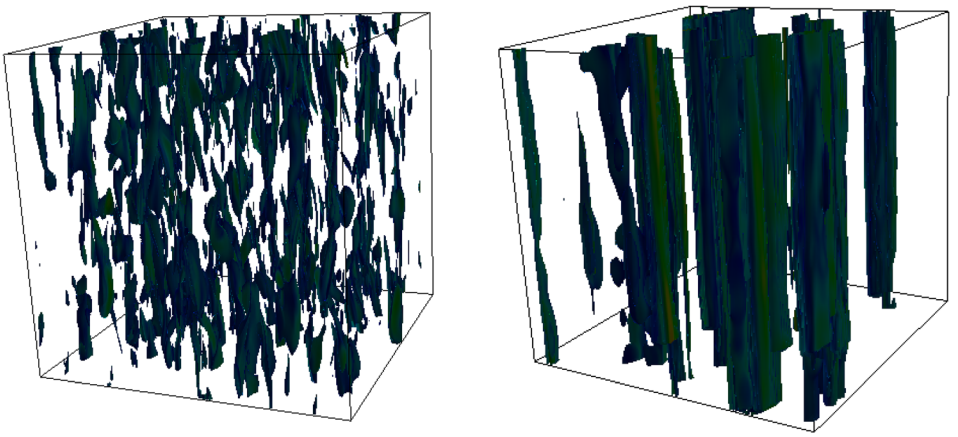

FIG. 1. Isosurfaces of magnitudes of vorticity $|\boldsymbol{\omega}|$ for mean magnetic field (a) $B_0 = 2$ and (b) $B_0 = 10$.

the vorticity $|\boldsymbol{\omega}|$, where $\boldsymbol{\omega} = \nabla \times \mathbf{u}$. The flow has vortical columnar structures along B_0 that becomes stronger as B_0 is increased. To get further details of the flow structure, we make a horizontal section for the $B_0 = 10$ case. In Figure 2(a), we show the density plot of vorticity magnitude along with velocity vectors (u_x, u_y). The flow develops a strong vortical structure, with strong u_y and u_x components, while modes that vary along $\hat{z}$ are very weak. The reason for the formation of these structures is discussed in detail in Sec. IV).

To quantify the anisotropy of the flow, we propose the anisotropy measures A_u and A_b for the velocity and magnetic fields as

$$A_u = \frac{E_u^{\perp}}{2E_u^{\parallel}}; \quad A_b = \frac{E_b^{\perp}}{2E_b^{\parallel}}, \tag{3}$$

where $E_u^{\perp} = \langle u_x^2 + u_y^2 \rangle/2$ and $E_u^{\parallel} = \langle u_z^2 \rangle/2$, where the angular brackets stand for spatial average. The quantities $E_u^{\perp}$ and $E_u^{\parallel}$ represent the kinetic energies of the perpendicular and parallel components of the velocity field. Similar definitions are employed for the magnetic field. The anisotropy parameter $A_{u,b}$ measures the degree of anisotropy among the different components of the velocity and magnetic field. It is defined such that $A_{u,b} = 1$ for isotropic flow with $\langle u_x^2 \rangle = \langle u_y^2 \rangle = \langle u_z^2 \rangle$, but it deviates from unity for anisotropic flows. In Table I, we list A_u and A_b for the two runs. For $B_0 = 2$, both A_u and A_b are smaller than unity, i.e., $E_u^{\perp} < 2E_u^{\parallel}$ (due to the particular choice of forcing used), while for $B_0 = 10$, their magnitude is substantially higher than unity $(E_{\perp} > 2E_{\parallel})$ that as we shall show later is due to the presence of an inverse cascade: the flow is quasi two-dimensional, hence it exhibits a strong inverse cascade of kinetic energy leading to buildup of kinetic energy at large scales.

Further insight can be obtained by studying the distribution of energy among the different components and different modes in the Fourier space. For isotropic flows, the energies of all the modes and all components within a thin spherical shell in Fourier-space are statistically equal. Hence, sum of the energies of all the Fourier modes in a spherical shell of radius k is often reported as a one-dimensional energy spectrum $E(k)$. It provides information about the distribution of energy at different scales. The one-dimensional spectra for the velocity and the magnetic field are shown in Fig. 3. For the $B_0 = 10$ case, the kinetic energy peaks at the large scales while the magnetic fluctuations are suppressed. This is due to the presence of an inverse cascade of energy as discussed in Ref. 19 (further discussions in Sec. V). For $B_0 = 2$, the inverse cascade is reasonably weak, if at all. This is also consistent with the values of A_u and A_b (presented in Table I) for the two cases and is discussed in detail in Secs. IV and V.

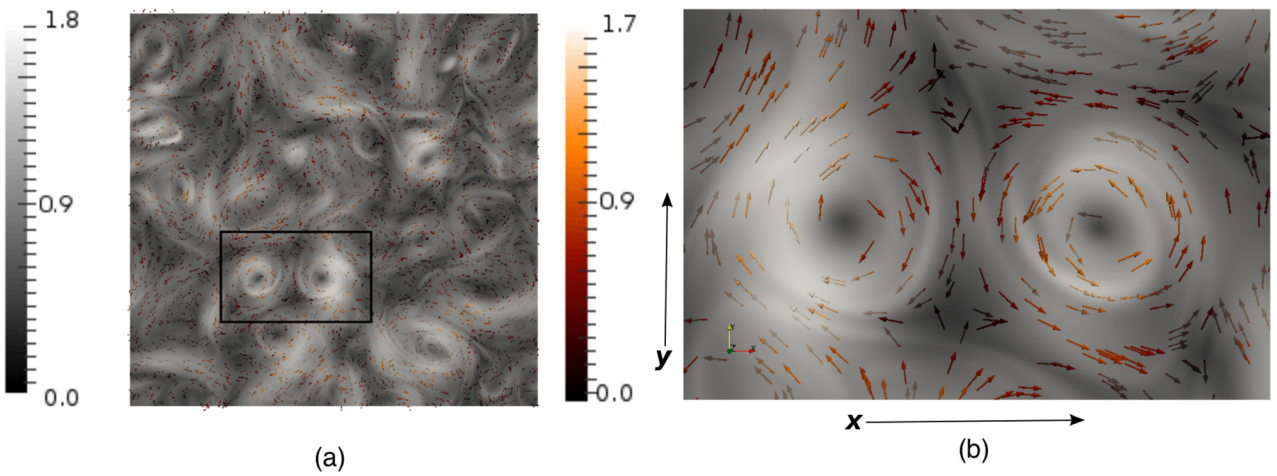

FIG. 2. For $B_0 = 10$, a horizontal cross-sectional view of (a) density plot of $|\boldsymbol{\omega}|$ (arrows) along with the velocity vectors (gray background), The "grayscale" and "hot-cold" (shown by "dark red/brown") colorcode correspond to the magnitude of velocity field and vorticity respectively. (b) A zoomed view of area inside the black rectangle of subplot (a).

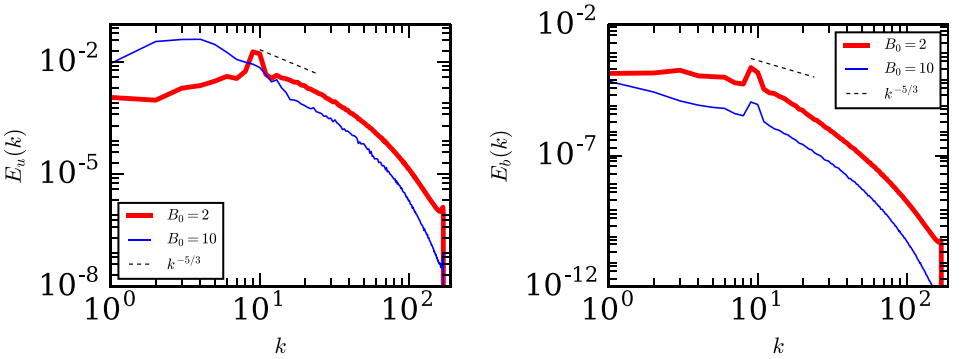

FIG. 3. Plots of (a) Kinetic energy spectrum, $E_u(k)$ and (b) Magnetic Energy Spectrum, $E_b(k)$ for $B_0 = 2$ and 10.

The dashed line indicates the $k^{-5/3}$ power-law scaling; our inertial range is too short to fit with this spectrum. As discussed in the introduction in this paper, our attempt is not to differentiate between the exponents $-3/2$ and $-5/3$, but rather study the effects of large B_0 on the global statistics of the flow.

To explore the nature of the anisotropy at different length scales, we work in the Fourier space, in which the equations are

$$\left(\frac{d}{dt} + \nu k^2\right) u_i(\mathbf{k}) - i(\mathbf{B}_0 \cdot \mathbf{k}) b_i(\mathbf{k}) = -ik_i P(\mathbf{k}) - ik_j \sum_{\mathbf{k}=\mathbf{p}+\mathbf{q}} u_j(\mathbf{q}) u_i(\mathbf{p}) + ik_j \sum_{\mathbf{k}=\mathbf{p}+\mathbf{q}} b_j(\mathbf{q}) b_i(\mathbf{p}) + \mathbf{f}(\mathbf{k}), \tag{4}$$

$$\left(\frac{d}{dt} + \eta k^2\right) b_i(\mathbf{k}) - i(\mathbf{B}_0 \cdot \mathbf{k}) u_i(\mathbf{k}) = -ik_j \sum_{\mathbf{k}=\mathbf{p}+\mathbf{q}} u_j(\mathbf{q}) b_i(\mathbf{p}) + ik_j \sum_{\mathbf{k}=\mathbf{p}+\mathbf{q}} b_j(\mathbf{q}) u_i(\mathbf{p}), \tag{5}$$

where $\hat{\mathbf{u}}(\mathbf{k}), \hat{\mathbf{b}}(\mathbf{k})$ are the Fourier transform of $\mathbf{u}$, $\mathbf{b}$ respectively. First we compute the wavenumber-dependent anisotropy parameters:

$$A_u(k) = \frac{E_u^{\perp}(k)}{2E_u^{\parallel}(k)}; \quad A_b(k) = \frac{E_b^{\perp}(k)}{2E_b^{\parallel}(k)}, \tag{6}$$

where $E_u^{\perp}(k)$ represents the sum of energy of the Fourier transform of $\mathbf{u}_{\perp}$ in the shell $(k-1:k]$. Similar definitions hold for other spectra. Figs. 4(a) and 4(b) exhibit the plots of $A_u(k)$ and $A_b(k)$ respectively. For $B_0 = 2$, $A_u(k) > 1$ for $k = 1$, and $A_u(k) \approx 1/2$ for $k > 1$. However for $B_0 = 10$, $A_u(k)$ is strongly anisotropic with $A_u(k) \gg 1$ for $k < k_f$, but $A_u(k) \ll 1$ for $k > k_f$. Thus, for $B_0 = 10$, the two-dimensional components in the large-scale velocity field dominate, consistent with the flow profile of Figs. 1 and 2. Note that $u_{\parallel}$ dominates over $u_{\perp}$ at large wavenumbers. This behavior is very similar to anisotropic behavior in quasi-static MHD reported by Reddy and Verma[20] and Favier *et al.*[28] For magnetic field $\mathbf{b}$, $A_b(k)$ is very large for $k = 1$, but $A_b(k) \sim 1$ for $1 < k < k_f$, while it is less than unity for $k > k_f$. The large peak at $k = 1$ for the ratio $E_b^{\perp}/E_b^{\parallel}$ is caused not due to excess of $E_b^{\perp}$ energy but rather due to the almost absence of $E_b^{\parallel}$ in the large scales. Indeed the quasi-2D motions of the flow are not able to amplify $E_b^{\parallel}$ and thus the ratio A_b almost diverges at $k = 1$. For Alfvenic turbulence where there is only a forward cascade, it is observed that $|\delta B_{\perp}|^2 \gg |\delta B_{\parallel}|^2$ (see Refs. 29 and 30). However, in our case, as we explain later in our text part of $E_u^{\perp}$ and $E_b^{\perp}$ cascades inversely, while $E_u^{\parallel}$ and $E_b^{\parallel}$ cascade forward causing an excess of $E_b^{\parallel}$ and $E_u^{\parallel}$ in the small scales.

A different measure of anisotropy is provided by looking at the distribution of energy in spectral space using a ring decomposition shown in Fig. 5 that we now discuss. A spherical shell in Fourier space is divided into rings such that each ring is characterized by two indices—the shell index k, and the sector index β.[20,24] The energy spectrum of a ring, called the *ring spectrum*, is defined as

$$E(k,\beta) = \frac{1}{C_\beta} \sum_{\substack{k-1 < k' \le k; \\ \zeta_{\beta-1} < \angle(\mathbf{k}') \le \zeta_\beta}} \frac{1}{2} |\hat{\mathbf{u}}(\mathbf{k}')|^2, \tag{7}$$

where $\angle \mathbf{k}'$ is the angle between $\mathbf{k}'$ and the unit vector $\hat{z}$, and the sector β contains the modes between the angles $\zeta_{\beta-1}$ to ζ_β. When $\Delta\zeta$ is uniform, the sectors near the equator contain more modes than those near the poles. Hence, to compensate

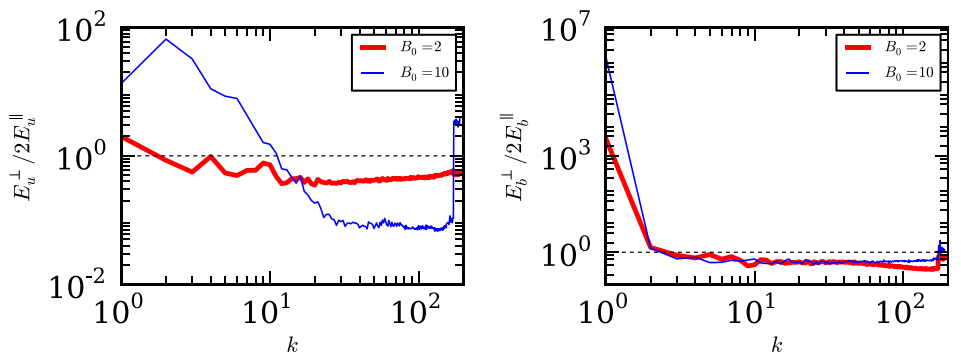

FIG. 4. Plots of anisotropy spectrum of the velocity field $A_u(k) = \frac{E_u^{\perp}(k)}{2E_u^{\parallel}(k)}$ and magnetic field $A_b(k) = \frac{E_b^{\perp}(k)}{2E_b^{\parallel}(k)}$.

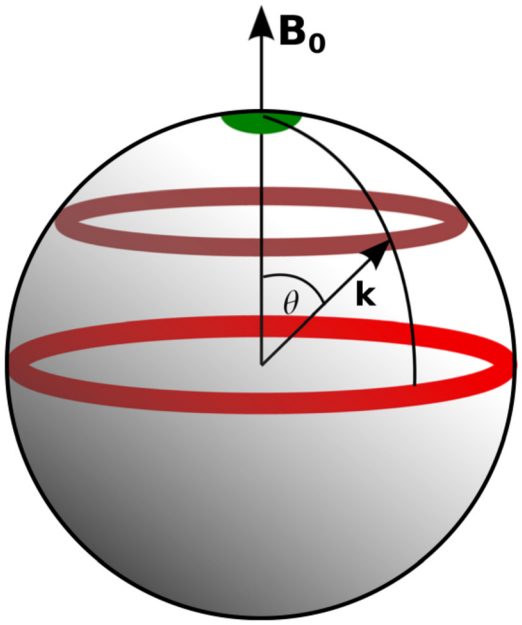

FIG. 5. Illustration of the ring decomposition in the spectral space. This figure is taken from Ref. 21. [Reprinted with permission from Phys. Plasmas **21**, 102310 (2014). Copyright 2014 AIP Publishing LLC].

for the above, we divide the sum $\sum_k |\hat{\mathbf{u}}(\mathbf{k}')|^2/2$ by the factor $C(\beta)$ given by

$$C_\beta = |\cos(\zeta_{\beta-1}) - \cos(\zeta_\beta)|. \tag{8}$$

For the ring spectrum computations, we divide the spectral space in the "northern" hemisphere into thin shells of unit widths (see Eq. (7)), which are further subdivided into 15 thin rings from $\theta = 0$ to $\theta = \pi/2$. For the ring spectrum, we vary k from 1 to $512 \times (2/3) = 341$; the factor 2/3 arising due to aliasing. Taking benefit of the $\theta \to (\pi - \theta)$ symmetry, we do not compute the energy of the rings in the "southern" hemisphere. In Fig. 6, we show the density plots of the kinetic and magnetic ring spectrum $E(k, \beta)$ for $B_0 = 2$ and 10. From the plots, it is evident that the kinetic and magnetic energy is stronger near the equator than the polar region, and the anisotropy increases with B_0. The anisotropy is greater for $B_0 = 10$, but the energy is concentrated near the equator even for $B_0 = 2$.

For further illustration, in Fig. 7, we show the normalized ring spectra $E(k, \theta)/E(k = 20)$ vs. θ for $B_0 = 2$ and 10 for $k = 20$, which is a generic wavenumber in the inertial range. Clearly $E(k, \theta)$, which is strongest for $\theta = \pi/2$, deviates strongly from a constant value, indicating anisotropy of the flow. The deviation is stronger for $B_0 = 10$ than $B_0 = 2$, which is consistent with the earlier discussion.

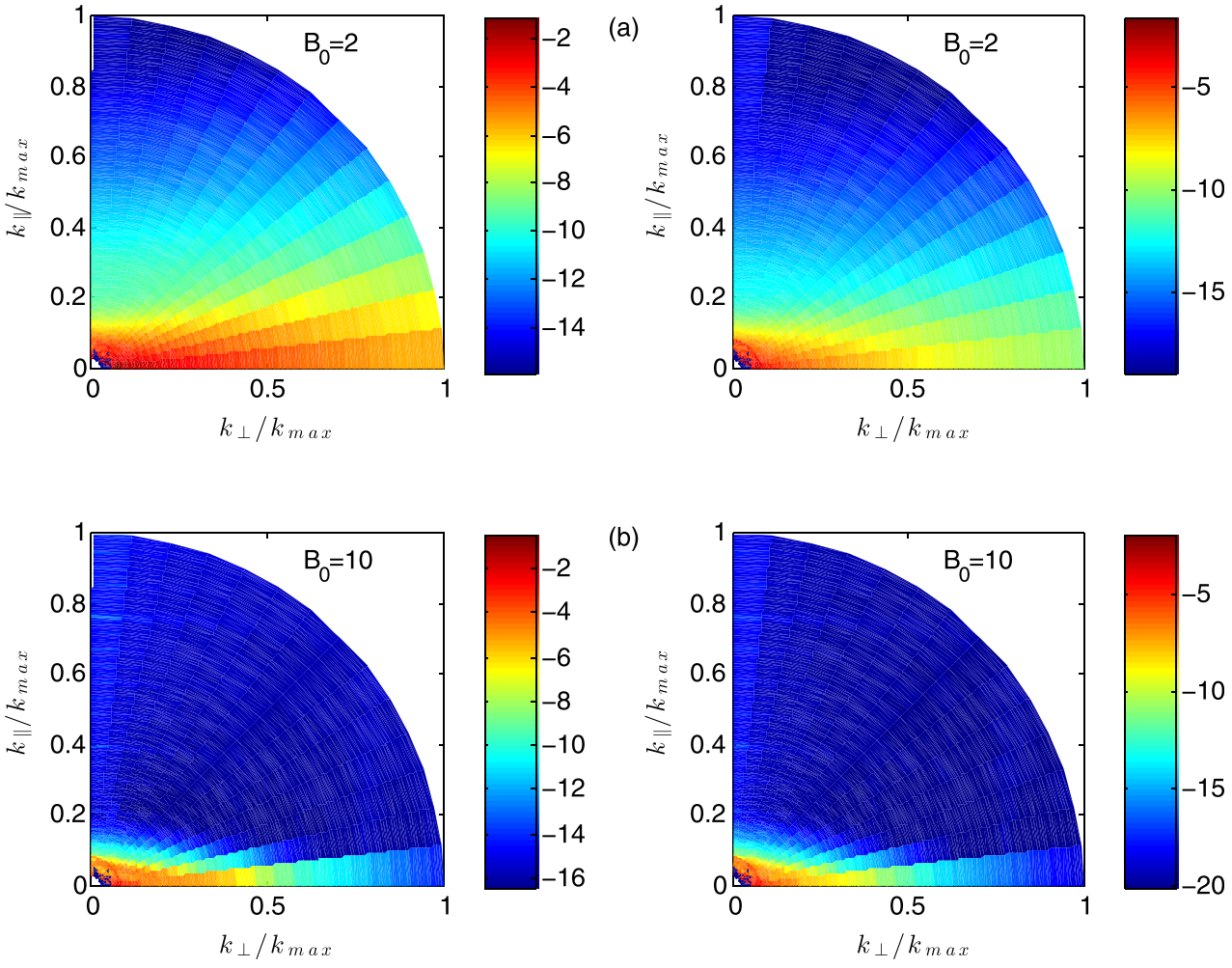

FIG. 6. The ring spectra in log scale: $\log(E_u(k, \theta))$ (left) and $\log(E_b(k, \theta))$ (right) for (a) $B_0 = 2$ and (b) $B_0 = 10$.

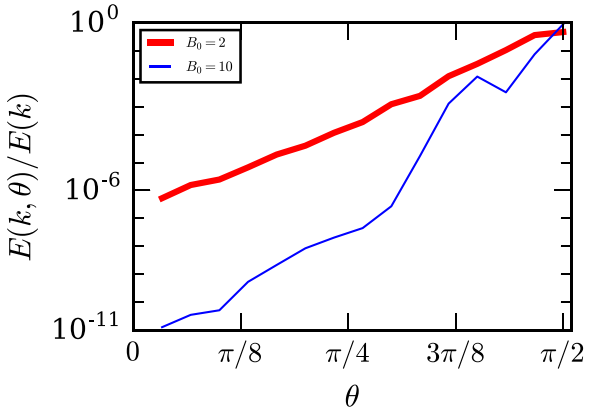

FIG. 7. Plot of $E(k=20,\theta)/E(k=20)$ vs. θ for (a) $B_0=2$ (thick line) and (b) $B_0=10$ (thin line).

IV. ENERGY FLUX AND SHELL-TO-SHELL ENERGY TRANSFERS

In this section, we will study the energy transfers that provide insights into the two-dimensionalization process in MHD turbulence. To delve into the anisotropy of the flow and its causes, we investigate the energy flux and energy exchange between the perpendicular and parallel components of the velocity field. Earlier, energy transfers in the Fourier space have been studied in detail by various groups.[8,31–33] Herein, we present an in-depth investigation of the energy transfers with comparatively stronger mean magnetic field amplitudes.

In hydrodynamics, for a basic triad of interacting wavenumbers (**k**, **p**, **q**) that satisfy $\mathbf{k}=\mathbf{p}+\mathbf{q}$, the mode-to-mode energy transfer rate from the mode **p** to the mode **k** via mediation of the mode **q** is given by

$$S(\mathbf{k}\,|\,\mathbf{p}\,|\,\mathbf{q}) = \Im\{[\mathbf{k}\cdot\hat{\mathbf{u}}(\mathbf{q})][\hat{\mathbf{u}}(\mathbf{p})\cdot\hat{\mathbf{u}}^*(\mathbf{k})]\}, \tag{9}$$

where $\Im$ and * denote respectively the imaginary part and complex conjugate of a complex number. To investigate the energy transfer rate from a set of wave numbers $\mathcal{D}_p$ to a set of wave numbers $\mathcal{D}_k$ we sum over all the possible triads $\mathbf{k}=\mathbf{p}+\mathbf{q}$

$$\mathcal{T}(\mathcal{D}_k,\mathcal{D}_p) = \sum_{\mathbf{k}\in\mathcal{D}_k}\sum_{\mathbf{p}\in\mathcal{D}_p} S(\mathbf{k}\,|\,\mathbf{p}\,|\,\mathbf{q}) = -\int[\mathbf{u_k}(\mathbf{u}\cdot\nabla)]\mathbf{u_p}dx^3, \tag{10}$$

where $\mathbf{u_k}(\mathbf{x}), \mathbf{u_p}(\mathbf{x})$ express the velocity field filtered so that only the modes in $\mathcal{D}_k, \mathcal{D}_p$ are kept respectably. The energy flux $\Pi(k_0)$ then can be defined as the rate of energy transfer from the set $\mathcal{D}_s$ of modes inside a sphere of radius k_0 to modes outside the same sphere, i.e.,

$$\Pi(k_0) = \sum_{k<k_0}\sum_{p\geq k_0} S(\mathbf{k}\,|\,\mathbf{p}\,|\,\mathbf{q}). \tag{11}$$

Similarly, we can define the shell-to-shell energy transfer rate $T_n^m = \mathcal{T}(\mathcal{D}_n,\mathcal{D}_m)$ as the energy transfer rate from the modes in a spherical shell $\mathcal{D}_m$ to the modes in the spherical shell $\mathcal{D}_n$.

MHD turbulence has six kinds of energy fluxes, namely, the energy flux from inner u-sphere to outer u-sphere ($\Pi_{u>}^{u<}(k_0)$), energy flux from inner u-sphere to outer b-sphere ($\Pi_{b>}^{u<}(k_0)$), energy flux from inner b-sphere to outer b-sphere ($\Pi_{b>}^{b<}(k_0)$), energy flux from inner b-sphere to outer u-sphere ($\Pi_{u>}^{b<}(k_0)$), energy flux from inner u-sphere to inner b-sphere ($\Pi_{b<}^{u<}(k_0)$), and energy flux from outer u-sphere to outer b-sphere ($\Pi_{b>}^{u>}(k_0)$). These fluxes can be computed using the following formulae:[8,31–34]

$$\begin{aligned}
\Pi_{u>}^{u<}(k_0) &= \sum_{k<k_0}\sum_{p\leq k_0}\Im\{[\mathbf{k}\cdot\hat{\mathbf{u}}(\mathbf{q})][\hat{\mathbf{u}}(\mathbf{p})\cdot\hat{\mathbf{u}}^*(\mathbf{k})]\} = +\int\mathbf{u}_k^<(\mathbf{u}\cdot\nabla)\mathbf{u}_k^>dx^3,\\
\Pi_{b>}^{u<}(k_0) &= -\sum_{k<k_0}\sum_{p\leq k_0}\Im\{[\mathbf{k}\cdot\hat{\mathbf{b}}(\mathbf{q})][\hat{\mathbf{u}}(\mathbf{p})\cdot\hat{\mathbf{b}}^*(\mathbf{k})]\} = -\int\mathbf{u}_k^<(\mathbf{b}\cdot\nabla)\mathbf{b}_k^>dx^3,\\
\Pi_{u>}^{b<}(k_0) &= -\sum_{k<k_0}\sum_{p\leq k_0}\Im\{[\mathbf{k}\cdot\hat{\mathbf{b}}(\mathbf{q})][\hat{\mathbf{b}}(\mathbf{p})\cdot\hat{\mathbf{u}}^*(\mathbf{k})]\} = -\int\mathbf{b}_k^<(\mathbf{b}\cdot\nabla)\mathbf{u}_k^>dx^3,\\
\Pi_{b>}^{b<}(k_0) &= \sum_{k<k_0}\sum_{p\leq k_0}\Im\{[\mathbf{k}\cdot\hat{\mathbf{u}}(\mathbf{q})][\hat{\mathbf{b}}(\mathbf{p})\cdot\hat{\mathbf{b}}^*(\mathbf{k})]\} = +\int\mathbf{b}_k^<(\mathbf{u}\cdot\nabla)\mathbf{b}_k^>dx^3,
\end{aligned} \tag{12}$$

where $\mathbf{u}_k^<, \mathbf{b}_k^<$ express the velocity and magnetic fields where only the modes inside a sphere of radius k are kept while $\mathbf{u}_k^>, \mathbf{b}_k^>$ express the velocity and magnetic fields where only the modes outside the same sphere are kept. The total energy flux, which is the total energy transfer from the modes inside the sphere to the modes outside the sphere, is

$$\Pi(k_0) = \Pi_{u>}^{u<}(k_0) + \Pi_{b>}^{u<}(k_0) + \Pi_{u>}^{b<}(k_0) + \Pi_{b>}^{b<}(k_0). \tag{13}$$

In the present paper, we compute the energy fluxes for 19 concentric spheres with their centres at k = (0, 0, 0). The radii of the first three spheres are 2, 4, and 8, and those of the last two spheres are $r_{\max-1}=170.5$ and $r_{\max}=512\times2/3=341$. Here, the factor 2/3 is introduced due to dealiasing. The intermediate shells are based on the powerlaw expression

$$r_i = r_3\left[\frac{r_{\max}}{16.0}\right]^{\frac{i-3}{n-4}}, \tag{14}$$

where $r_3=8$ is radius of the third sphere, $r_{\max}$ is the radius of the last sphere, and $n=19$ is the total number of spheres.

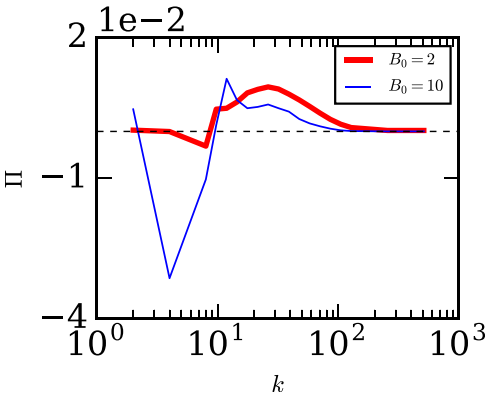

FIG. 8. Plot of the total energy flux $\Pi(k)$ vs. k.

Hence, the radii of the spheres are 2.0, 4.0, 8.0, 9.8, 12.0, 14.8, 18.1, 22.2, 27.2, 33.4, 40.9, 50.2, 61.5, 75.4, 92.5, 113.4, 139.0, 170.5, and 341.0. In the inertial range, we bin the radii of the shells logarithmically keeping in mind the powerlaw physics observed here. The inertial range however is too short since the forcing band is shifted to $k = [8, 10]$.

For $B_0 = 2$ and 10, the total energy flux is shown in Fig. 8, while the individual fluxes (see Eq. (12)) are exhibited in Fig. 9. The plots are for a given snapshot during the evolved state. Due to aforementioned reason (lack of averaging) and relatively smaller resolution, we do not observe constant energy fluxes.

The most noticeable feature of the plots is the dominance of the inverse cascade of $\Pi^{u<}_{u>}(k_0)$ for $k < k_f$ when $B_0 = 10$. This result is due to the quasi two-dimensionalization of the flow, and it is consistent with a large kinetic energy at the large-scales near the equatorial region, discussed in Section III. The other energy fluxes are several orders of magnitudes smaller than the maximum value of $\Pi^{u<}_{u>}(k_0)$.

In addition to the inverse cascade of kinetic energy, we observe that for $k > k_f$, all the energy fluxes are positive, which is consistent with the earlier results by Debliquy *et al.*[33] for $B_0 = 0$. Interestingly, $\Pi^{b<}_{b>} < 0$ for small wavenumbers ($k < k_f$) indicating an inverse cascade of magnetic energy as well. It is important to note however that for $k > k_f$, $\Pi^{u<}_{u>}(k_0)$ is the most dominant flux, and it is positive. This is in contrast to the two-dimensional fluid turbulence in which the kinetic energy flux $\Pi^{u<}_{u>} \approx 0$ for $k > k_f$. The above feature is due to the forward energy transfer of $u_\parallel$.

For anisotropic flows, Reddy *et al.*[21] showed how to compute the energy fluxes for the parallel and perpendicular components of the velocity fields. They showed that these fluxes are

$$\Pi^u_\parallel = \sum_{k<k_0} \sum_{p>k_0} S_\parallel(\mathbf{k}|\mathbf{p}|\mathbf{q}), \tag{15}$$

$$\Pi^u_\perp = \sum_{k<k_0} \sum_{p>k_0} S_\perp(\mathbf{k}|\mathbf{p}|\mathbf{q}), \tag{16}$$

where

$$S^u_\parallel(\mathbf{k}|\mathbf{p}|\mathbf{q}) = \Im\{\left[\mathbf{k}\cdot\hat{\mathbf{u}}(\mathbf{q})\right]\left[\hat{u}^*_\parallel(\mathbf{k})\hat{u}_\parallel(\mathbf{p})\right]\}, \tag{17}$$

$$S^u_\perp(\mathbf{k}|\mathbf{p}|\mathbf{q}) = \Im\{\left[\mathbf{k}\cdot\hat{\mathbf{u}}(\mathbf{q})\right]\left[\hat{\mathbf{u}}^*_\perp(\mathbf{k})\cdot\hat{\mathbf{u}}_\perp(\mathbf{p})\right]\}, \tag{18}$$

where $\Im$ and * stand for the imaginary and complex conjugate of the arguments. Note that $\Pi^{u<}_{u>} = \Pi^u_\parallel + \Pi^u_\perp$. It is easy to derive the corresponding formulae for the magnetic energy by replacing $\hat{u}_\parallel$ and $\hat{\mathbf{u}}_\perp$ in Eqs. (17) and (18) by $\hat{b}_\parallel$ and $\hat{\mathbf{b}}_\perp$ respectively. In this paper, we report the above fluxes only for the velocity field since the magnetic energy is much smaller than the kinetic energy. In Fig. 10, we plot $\Pi^u_\parallel$ that exhibits a forward energy cascade of $u_\parallel$ at large

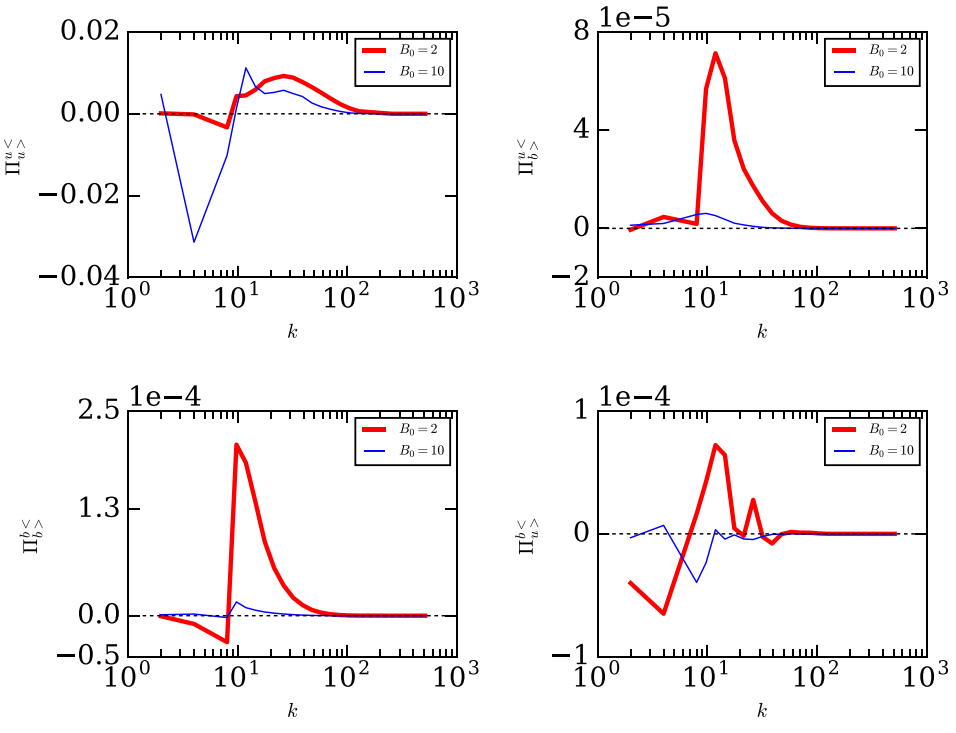

FIG. 9. Plots of energy fluxes $\Pi^{u<}_{u>}$, $\Pi^{u<}_{b>}$, $\Pi^{b<}_{b>}$, and $\Pi^{b<}_{u>}$ *vs.* k.

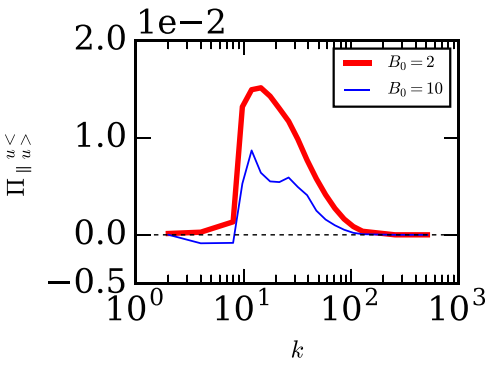

FIG. 10. Plot of the energy flux $\Pi_{\parallel}^{u}$ of the parallel component of the velocity field, $u_{\parallel}$.

wavenumbers. The energy flux of the perpendicular component, $\Pi_{\perp}^{u}$ (not shown here), exhibits an inverse cascade. The above observation is very similar to the quasi two-dimensional behaviour reported for quasi-static MHD turbulence by Reddy *et al.*[21] and Favier *et al.*[28]—$\hat{\mathbf{u}}_{\perp}$ exhibiting an inverse cascade at low wavenumbers, while $u_{\parallel}$ a forward cascade at large wavenumbers. We further note that kinetic helicity $H = \langle \mathbf{u} \cdot \nabla \times \mathbf{u} \rangle$ in this quasi two-dimensional is a result of the correlation of the vertical velocity and the two dimensional vorticity $w_z = \partial_x u_y - \partial_y u_x$ thus the forward cascade of helicity is controlled by the forward cascade of energy of the vertical component. The forward cascade of Helicity has been shown recently to alter the exponent of the energy spectrum.[35]

However $E_u^{\perp}$ and $E_u^{\parallel}$ are not independently conserved quantities. $E_u^{\perp}$ energy can be transferred to $E_u^{\parallel}$ and vice versa via pressure. This transfer can be quantified by

$$\mathcal{P}_{\parallel}(\mathbf{k}) = \Im\{[k_{\parallel}\hat{u}_{\parallel}(\mathbf{k})]P(\mathbf{k})\}, \tag{19}$$

as shown in Ref. 21. A sum of the above over a wavenumber shell yields the energy transfer from $\mathbf{u}_{\perp}$ to $u_{\parallel}$ for that shell. The above energy transfer, plotted in Fig. 11, reveals that this energy transfer is relatively weak for $B_0 = 10$. This feature may be due to a relatively weak pressure and velocity fields. The energy transfer from $\mathbf{u}_{\perp}$ to $u_{\parallel}$ enhances $E_u^{\parallel}$, which is advected to larger wavenumbers. Such features have been observed for the quasi-static MHD.[21] The energy of the perpendicular component ($E_u^{\perp}$) however grows in large scales in the presence of an inverse cascade. This is not very significant for $B_0 = 2$ that has no inverse cascade, but it is dominant

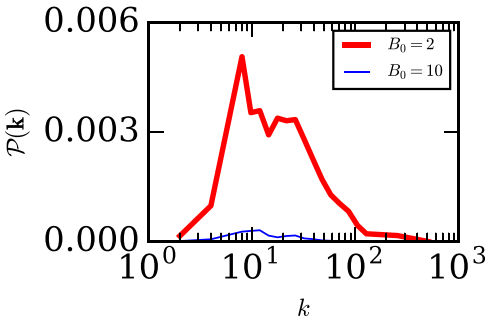

FIG. 11. Plot of $\mathcal{P}_{\parallel}(\mathbf{k})$, the energy transfer rate from $u_{\perp}$ to $u_{\parallel}$ via pressure.

for $B_0 = 10$. Thus, $E_u^{\parallel} \sim E_u^{\perp}$ for $B_0 = 2$, but $E_u^{\parallel} \ll E_u^{\perp}$ for $B_0 = 10$ (see Table I). As described above and exhibited in Fig. 10, $u_{\parallel}$ cascades forward to larger wavenumbers, which is the cause for the $A_u(k) = E_u^{\perp}(k)/(2E_u^{\parallel}(k)) < 1$ for large k. We also observe that the energy transfers for the magnetic field may be coupled to the above transfers of kinetic energy; this aspect needs to be investigated in detail.

The energy flux describes the net energy emanating from a sphere. More details on energy transfer are revealed by the shell-to-shell energy transfer rates. For fluid turbulence, we have shell-to-shell transfers for the velocity field. However, for MHD turbulence, we have velocity-to-velocity (*U2U*), magnetic-to-magnetic (*B2B*), and kinetic-to-magnetic (*U2B*) shell-to-shell energy transfers.[24,31–33] The energy transfer from wavenumber shell m of field X to wavenumber shell n of field Y is defined as (X, Y are either velocity or magnetic field)

$$\begin{aligned}
\mathcal{T}_{n,m}^{u,u} &= \sum_{k\in\mathcal{D}_n}\sum_{p\in\mathcal{D}_m} \Im\{[\mathbf{k}\cdot\hat{\mathbf{u}}(\mathbf{q})][\hat{\mathbf{u}}(\mathbf{p})\cdot\hat{\mathbf{u}}^*(\mathbf{k})]\} \\
&= -\int [\mathbf{u}_{\mathbf{k}}(\mathbf{u}\cdot\nabla)]\mathbf{u}_{\mathbf{p}}dx^3, \qquad (20)\\
\mathcal{T}_{n,m}^{b,b} &= \sum_{k\in\mathcal{D}_n}\sum_{p\in\mathcal{D}_m} \Im\{[\mathbf{k}\cdot\hat{\mathbf{u}}(\mathbf{q})][\hat{\mathbf{b}}(\mathbf{p})\cdot\hat{\mathbf{b}}^*(\mathbf{k})]\} \\
&= -\int [\mathbf{b}_{\mathbf{k}}(\mathbf{u}\cdot\nabla)]\mathbf{b}_{\mathbf{p}}dx^3, \qquad (21)\\
\mathcal{T}_{n,m}^{b,u} &= -\sum_{k\in\mathcal{D}_n}\sum_{p\in\mathcal{D}_m} \Im\{[\mathbf{k}\cdot\hat{\mathbf{u}}(\mathbf{q})][\hat{\mathbf{u}}(\mathbf{p})\cdot\hat{\mathbf{b}}^*(\mathbf{k})]\} \\
&= +\int [\mathbf{b}_{\mathbf{k}}(\mathbf{b}\cdot\nabla)]\mathbf{u}_{\mathbf{p}}dx^3. \qquad (22)
\end{aligned}$$

For the shell-to-shell energy transfers, we divide the wavenumber space into 19 concentric shells with their centres at k = (0, 0, 0). The inner and outer radii of the nth shell are k_{n-1} and k_n, respectively, where $k_n = 0$, 2.0, 4.0, 8.0, 9.8, 12.0, 14.8, 18.1, 22.2, 27.2, 33.4, 40.9, 50.2, 61.5, 75.4, 92.5, 113.4, 139.0, 170.5, and 341.0. The aforementioned radii are chosen using the same algorithm as those used for computing the radii of the spheres for flux computations. In Fig. 12, we present the shell-to-shell energy transfer rates, T_{nm}^{uu}, T_{nm}^{bb}, and T_{nm}^{bu} for $B_0 = 2$ (left column) and $B_0 = 10$ (right column).

The *U2U* and *B2B* transfers for $B_0 = 2$, exhibited in Fig. 12(a) is similar to those reported by Alexakis *et al.*,[32] Debliquy *et al.*,[33] and Carati *et al.*[36] for $B_0 = 0$ forward and local *U2U* and *B2B* transfers, that is, the most energy transfers are from shell $m - 1$ to shell m. The *U2B* transfer is from shell m of the velocity field to shell m of the magnetic field, which is because the velocity field dominates the magnetic field;[33] this feature is exactly opposite to that of $B_0 = 0$ (Refs. 32, 33, and 36) because $E_b > E_u$ for the $B_0 = 0$ case.

For $B_0 = 10$ (see Fig. 12), *U2U* is the most dominant transfer, and the *U2U* and *B2B* shell-to-shell transfer exhibits inverse energy transfers for the 3rd and 4th shell ($k < k_f$), i.e., from the 4th shell to the 3rd shell. This result is consistent with the inverse cascades of kinetic and magnetic energies for $k < k_f$ (see Fig. 9). The *U2B* transfers are nonzero only for $k < k_f$.

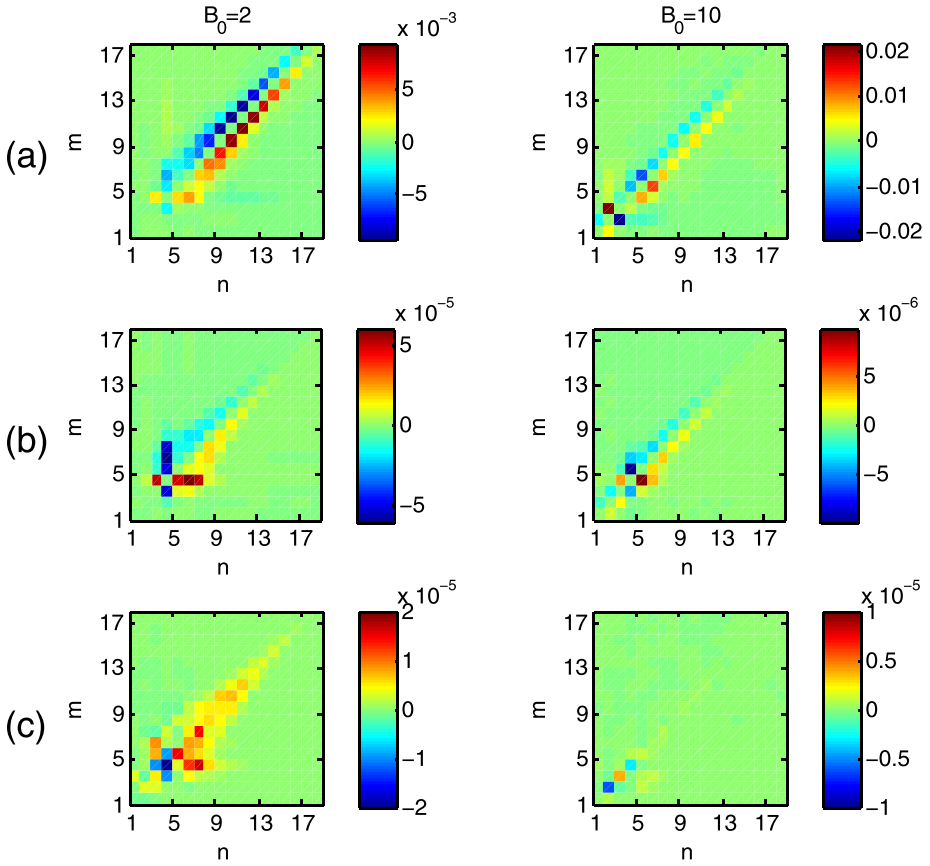

FIG. 12. Shell-to-shell energy transfers (a) *U2U*, (b) *B2B*, and (c) *U2B* for $B_0 = 2$ (left column) and $B_0 = 10$ (right column). Here m is the giver shell, and n is the receiver shell.

V. SUMMARY AND DISCUSSION

In this paper, we analyzed the anisotropy induced by a constant magnetic field in MHD turbulence. Here we provide a semiquantitative picture of the above phenomena. Shear Alfvén modes are linear excitations of MHD flows, and they are governed by equations

$$\frac{d\hat{\mathbf{u}}(\mathbf{k})}{dt} = i(\mathbf{B}_0 \cdot \mathbf{k})\hat{\mathbf{b}}(\mathbf{k}); \quad \frac{d\hat{\mathbf{b}}(\mathbf{k})}{dt} = i(\mathbf{B}_0 \cdot \mathbf{k})\hat{\mathbf{u}}(\mathbf{k}). \tag{23}$$

The above equations have valid wave solutions when $\mathbf{B}_0 \cdot \mathbf{k} \neq 0$, that is, for wave vectors off from the plane perpendicular to the mean magnetic field. For such modes, in Eqs. (4) and (5), $(\mathbf{B}_0 \cdot \mathbf{k})\mathbf{u}(\mathbf{k})$ and $(\mathbf{B}_0 \cdot \mathbf{k})\mathbf{b}(\mathbf{k})$ dominates the nonlinear term. Earlier, Galtier *et al.*[18] had analysed the weak turbulence limit of MHD turbulence for large B_0 and showed that $E(k_\perp) \sim k_\perp^{-2}$.

For the Fourier modes with $k_\parallel = 0$, the linear terms dropout of Eqs. (4) and (5) and the nonlinear terms dominate the flow with dynamics. In addition, for large B_0, $b^2 \ll u^2$ (see Table I). Since $k_\parallel = 0$ for such modes, the modes have interactions similar to two-dimensional hydrodynamic turbulence. These interactions lead to two-dimensionalization of the flow. The reason for $b^2 \ll u^2$ is not obvious at present. It may be due to the absence of shear Alfvén waves for modes with $k_\parallel = 0$. To sum up, for the Fourier modes with $k_\parallel \neq 0$, we obtain Alfvénic fluctuations, which are described by Eq. (23) in the linear limit. However, for large B_0, the fluctuations corresponding to these modes are weak compared to the vortical structures. Thus the flow is dominated by the $k_\parallel = 0$ modes. These arguments provide a qualitative picture for the emergence of quasi two-dimensional vortices in MHD turbulence with strong B_0. The above behaviour has strong similarities with the vortical structures observed in rotating and quasi-static MHD turbulence.[20]

The dominance of these modes leads then to an anisotropic distribution of the velocity components with the perpendicular components dominating in large scales due to the inverse cascade of $E_\perp$ while the parallel components dominate in small scales due to the forward cascade of $E_\parallel$. This leads to the formation of the observed vortical structures.

In summary, we show how strong mean magnetic field makes the MHD turbulence quasi two-dimensional. This conclusion is borne out in the global-energy anisotropy parameter, ring spectrum, energy flux, and shell-to-shell energy transfers. The flow has strong similarities with those observed in rotating and quasi-static MHD turbulence. Detailed dynamical connections between these flows need to be explored in a future work.

ACKNOWLEDGMENTS

We thank Sandeep Reddy, Abhishek Kumar, Biplab Dutta, and Rohit Kumar for valuable discussions. Our numerical simulations were performed at HPC2013 and Chaos clusters of IIT, Kanpur. This work was supported by the research Grant No. 4904-A from Indo-French Centre for the Promotion of Advanced Research (IFCPAR/CEFIPRA), SERB/F/3279/2013-14 from the Science and Engineering Research Board, India. S. Sundar is supported by Christian-Albrechts-Universität zu Kiel and by the Deutsche Forschungsgemeinschaft via SFB-TR 24.

[1]A. Alexakis, Phys. Rev. Lett. **110**, 084502 (2013).
[2]P. S. Iroshnikov, Sov. Astron. **40**, 742 (1963).
[3]R. H. Kraichnan, Phys. Fluids **8**, 1385 (1965).
[4]J. V. Shebalin, W. H. Matthaeus, and D. Montgomery, J. Plasma Phys. **29**, 525 (1983).
[5]G. P. Zank and W. Matthaeus, Phys. Fluids A: Fluid Dyn. **5**, 257 (1993).
[6]S. Oughton, E. R. Priest, and W. H. Matthaeus, J. Fluid Mech. **280**, 95 (1994).
[7]M. K. Verma, Phys. Plasmas **6**, 1455 (1999).
[8]M. K. Verma, Phys. Rep. **401**, 229 (2004).
[9]M. Verma, Phys. Rev. E **64**, 26305 (2001).
[10]P. Goldreich and S. Sridhar, Astrophys. J. **438**, 763 (1995).
[11]S. Boldyrev, Phys. Rev. Lett. **96**, 115002 (2006).
[12]S. Boldyrev and J. C. Perez, Phys. Rev. Lett. **103**, 225001 (2009).
[13]J. C. Perez, J. Mason, S. Boldyrev, and F. Cattaneo, Phys. Rev. X **2**, 041005 (2012).
[14]J. C. Perez, J. Mason, S. Boldyrev, and F. Cattaneo, Astrophys. J. Lett. **793**, L13 (2014).
[15]A. Beresnyak and A. Lazarian, Astrophys. J. **702**, 1190 (2009).
[16]A. Beresnyak, Phys. Rev. Lett. **106**, 075001 (2011).
[17]A. Beresnyak, Astrophys. J. Lett. **784**, L20 (2014).
[18]S. Galtier, S. V. Nazarenko, A. C. Newell, and A. Pouquet, J. Plasma Phys. **63**, 447 (2000).
[19]A. Alexakis, Phys. Rev. E **84**, 056330 (2011).
[20]K. S. Reddy and M. K. Verma, Phys. Fluids **26**, 025109 (2014).
[21]K. S. Reddy, R. Kumar, and M. K. Verma, Phys. Plasmas **21**, 102310 (2014).
[22]B. Gallet and C. R. Doering, J. Fluid Mech. **773**, 154 (2015).
[23]A. Alexakis, B. Bigot, H. Politano, and S. Galtier, Phys. Rev. E **76**, 056313 (2007).
[24]B. Teaca, M. K. Verma, B. Knaepen, and D. Carati, Phys. Rev. E **79**, 046312 (2009).
[25]P. H. Roberts, *An Introduction to Magnetohydrodynamics* (Elsevier, New York, 1967).
[26]P. D. Mininni, D. Rosenberg, R. Reddy, and A. Pouquet, Parallel Comput. **37**, 316 (2011).
[27]M. K. Verma, A. Chatterjee, K. S. Reddy, R. K. Yadav, S. Paul, M. Chandra, and R. Samtaney, Pramana **81**, 617 (2013).
[28]B. Favier, F. S. Godeferd, C. Cambon, and A. Delache, Phys. Fluids **22**, 075104 (2010).
[29]J. M. TenBarge, J. J. Podesta, K. G. Klein, and G. G. Howes, Astrophys. J. **753**, 107 (2012).
[30]O. Alexandrova, V. Carbone, P. Veltri, and L. Sorriso-Valvo, Astrophys. J. **674**, 1153 (2008).
[31]G. Dar, M. K. Verma, and V. Eswaran, Physica D **157**, 207 (2001).
[32]A. Alexakis, P. D. Mininni, and A. Pouquet, Phys. Rev. E **72**, 046301 (2005).
[33]O. Debliquy, M. K. Verma, and D. Carati, Phys. Plasmas **12**, 042309 (2005).
[34]P. D. Mininni, A. G. Pouquet, and D. C. Montgomery, Phys. Rev. Lett. **97**, 244503 (2006).
[35]N. E. Sujovolsky and P. D. Mininni, Phys. Rev. Fluids **1**, 054407 (2016).
[36]D. Carati, O. Debliquy, B. Knaepen, B. Teaca, and M. K. Verma, J. Turbul. **7**, N51 (2006).